Int. J. Electrochem. Sci., 17 **(2022)** Article Number: 22033, doi: 10.20964/2022.03.08

International Journal of
ELECTROCHEMICAL
SCIENCE
www.electrochemsci.org

Structural Analysis of Nanocrystalline Cu_2O Prepared by Electrodeposition at Different Temperatures

Setia Budi[1,*], *Wisnu Ari Adi*[2,*], *Yusmaniar*[1], *Zahra Fairuza*[1], *Imam Basori*[3], *Akrajas Ali Umar*[4]

[1] Department of Chemistry, Faculty of Mathematics and Natural Sciences, Universitas Negeri Jakarta, Jl. Rawamangun Muka, Jakarta 13220, Indonesia
[2] National Research and Innovation Agency, Kawasan Puspiptek Serpong, Tangerang Selatan, Banten, Indonesia
[3] Department of Mechanical Engineering, Faculty of Engineering, Universitas Negeri Jakarta, Jl. Rawamangun Muka, Jakarta 13220, Indonesia
[4] Institute of Microengineering dan Nanoelectronics, Universiti Kebangsaan Malaysia, Selangor 43600, Malaysia
[*]E-mail: setiabudi@unj.ac.id, dwisnuaa@batan.go.id

Received: 19 Octoberr 2021 / *Accepted:* 9 December 2021 / *Published:* 2 February 2022

The results of structural and phase analyses of Cu_2O films electrodeposited at different temperatures are reported in this paper. The electrodeposition temperature was varied to obtain a single-phase Cu_2O film. Structural information and the phase composition were extracted from X-ray diffraction patterns using a general structure analysis system (GSAS) to perform Rietveld refinement. Increasing the deposition temperature decreased the crystallite size and increased the lattice strain in the films. A preferential orientation was found at relatively high deposition temperatures. The Cu_2O phase began to form above room temperature, and a single phase of nanocrystalline Cu_2O with a fine crystallite size of 34 nm was grown at a deposition temperature of 75°C. This pure Cu_2O film had a uniform surface morphology with a direct bandgap energy of 2.18 eV. These results show how temperature controls the structure and phase composition of electrodeposited Cu_2O.

Keywords: Structural and phase analysis, single-phase Cu_2O, electrodeposition temperature, general structure analysis system

1. INTRODUCTION

Cuprous oxide (Cu_2O) possesses unique optical and electrochemical properties among semiconductor materials. Cu_2O is also considered a low-cost, harmless, and environmentally friendly material with low toxicity [1]. These characteristics have made Cu_2O a promising candidate for various applications, such as photocatalysts [2,3], gas and optoelectronic sensors [4,5], and batteries [6,7]. The

optical and electrochemical properties of Cu_2O depend on the structure and purity of its phases [5,8]. In recent years, various preparation techniques have been used to synthesize a pure Cu_2O phase with desired material characteristics, including thermal oxidation [9], chemical vapor deposition [10], reactive sputtering [11], and electrodeposition [3,12,13].

Electrodeposition is a well-known low-cost electrochemical method that consists of employing a relatively simple device to prepare metals [14,15] and metal oxide [16] particles. The deposit characteristics can be modified by introducing additives [17–19] and adjusting the electrodeposition conditions, such as the pH, temperature, and applied current density [20–22]. The introduction of additives, such as $NaNO_3$, Na_2SO_4, NH_4NO_3, and $(NH_4)_2SO_4$, has been reported to modify Cu_2O crystals electrochemically deposited on different substrates. Although the cations of additives, for example Na^+, have no significant influence on deposit microstructures, the presence of SO_4^{2-} and NO_3^- anions can change the stability and growth of crystallographic fields of Cu_2O [23]. However, the preparation of pure Cu_2O films remains challenging due to the growth of additional phases, such as metallic Cu and CuO. Consequently, the effect of the conditions of the electrodeposition process on the phases grown on a substrate must be taken into account. The deposition temperature has been reported as a crucial parameter in the synthesis of structures. Nevertheless, no comprehensive study on the effect of the deposition temperature on structural changes in electrodeposited Cu_2O has been conducted.

In this study, the effect of electrodeposition temperatures on the deposit structures and phase composition of Cu_2O was evaluated. The Rietveld refinement method was employed with general structure analysis system (GSAS) software to perform the structural investigation. The nanocrystalline Cu_2O film was examined under a diffuse reflectance sphere to determine the energy bandgap of the electrodeposited semiconductor film.

2. MATERIALS AND METHOD

The materials used for sample preparation, namely, $CuSO_4.5H_2O$ and $(NH_4)_2SO_4$, were analytical grade chemicals supplied by Merck. Double-distilled water was used to prepare the electrolyte consisting of 0.025 M $CuSO_4.5H_2O$ and 0.2 M $(NH_4)_2SO_4$. Electrodeposition was carried out in a three-electrode cell using platinum wire and Ag/AgCl as the counter and reference electrodes, respectively. An indium tin oxide sheet with a deposition area of 10 x 20 mm was used as a substrate. The Cu_2O electrodeposition process was performed at various deposition temperatures (10, RT, 45, and 75°C) using an ER466 potentiostat controlled by EDAQ Chart software. The electrodeposited sample was rinsed with double-distilled water and dried at room temperature. Structural and phase analyses were conducted using an EMPYREAN PANalytical X-ray diffractometer. The XRD patterns of the films were analyzed using the Rietveld refinement method with GSAS software to determine the lattice parameters, unit cell volume, atomic density, and preferred orientation of the deposits [24–26]. The morphological study was carried out using a FEI field emission scanning electron microscope (FESEM). Optical analysis was carried out to determine the band gap energy (E_g) by recording UV–vis light reflection using a diffuse reflectance sphere in a Hitachi UV–vis spectrophotometer.

3. RESULTS AND DISCUSSION

Deposits were successfully prepared using an electrodeposition technique at different temperatures. The morphological features of the deposits determined by FESEM are shown in Figure 1. The FESEM micrograph showed that the deposit grown on the substrate consisted of layers with a uniform morphology, demonstrating the efficacy of the electrodeposition technique for the direct synthesis of metal and metal oxide. At the lower deposition temperatures of 10°C and RT, irregularly shaped deposits were observed. However, the micrograph in Figure 1c-d shows that cubic structures surrounded by irregularly shaped structures formed over these deposits, indicating the initial deposition orientation changed with increasing temperature. When electrodeposition was performed above room temperature, the morphology of the deposits changed to fine octahedral crystals with different exposed facets (Fig. 1e-f). Increasing the temperature to 75°C changed the deposit morphology, and compact deposits of Cu_2O formed (Fig. 1g-h). These results showed that the electrodeposition temperature modified the growth orientation of the crystal and produced Cu_2O deposits with different characteristics.

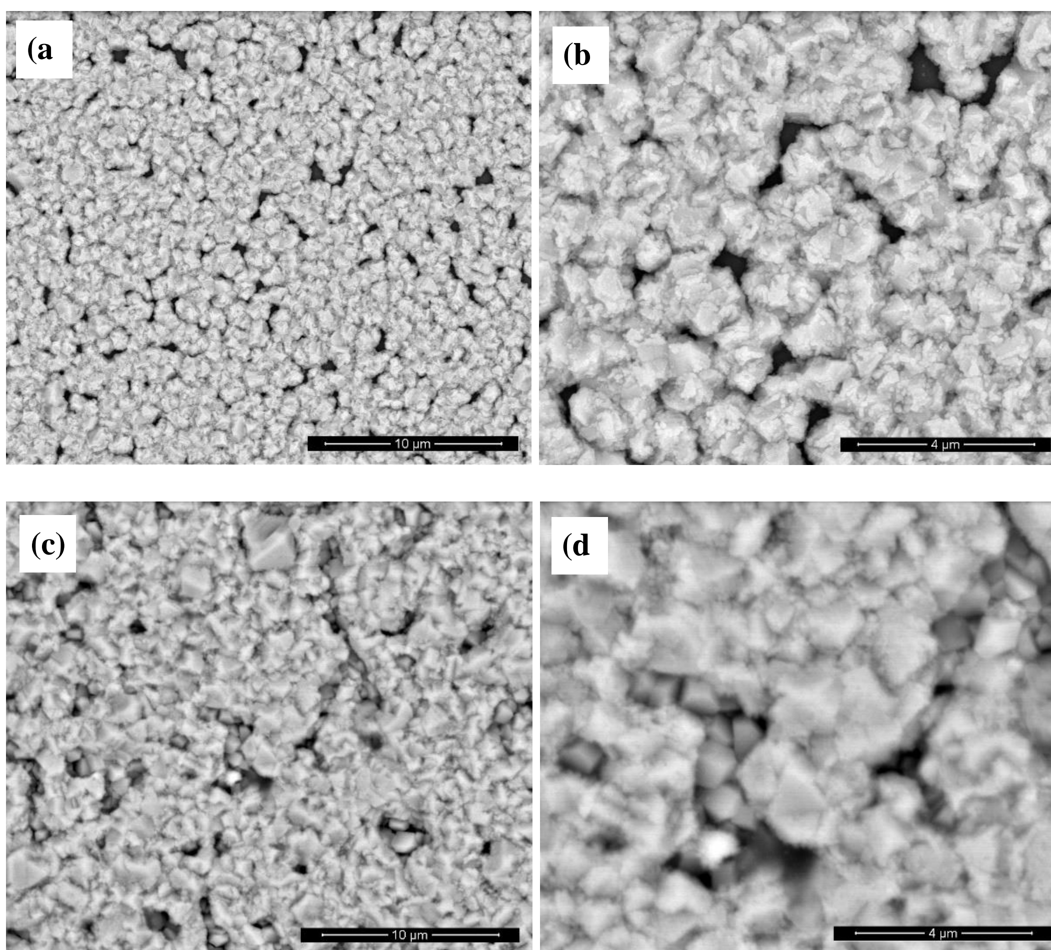

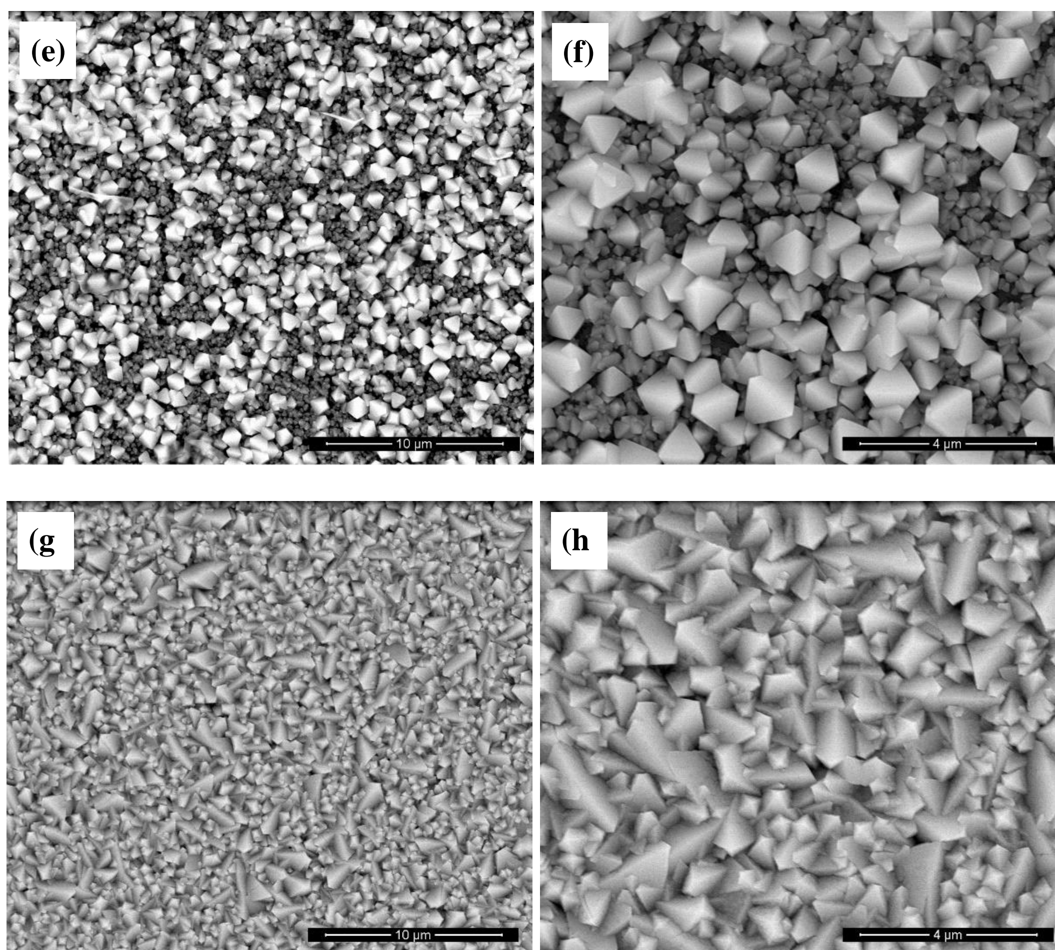

Figure 1. Micrographs of Cu_2O samples electrodeposited at deposition temperatures of 10°C (a-b), RT (c-d), 45°C (e-f), and 75°C (g-h).

An X-ray diffractometer was used to determine the phases and structures in the deposits. Figure 2a shows the XRD patterns formed from the electrodeposition of Cu_2O at different temperatures in a 2θ range from 30° to 90°. Peaks in the XRD patterns from crystalline phases of Cu and Cu_2O appeared together with those for the indium tin oxide substrate due to the formation of a thin deposit of Cu_2O. At deposition temperatures of 10°C and RT, in addition to the substrate peaks, several peaks appeared at 2θ values of 43.3°, 50.4°, 74.2°, and 89.9° corresponding to the (111), (200), (220), and (311) planes of the cubic structure of Cu, respectively. There was no diffraction peak that could be associated with Cu_2O. These patterns indicated that the Cu_2O phase did not form at these deposition temperatures. However, the intensity of the Cu peaks decreased with increasing temperature and then vanished at 75°C. At a deposition temperature of 45°C, diffraction patterns were obtained with peaks at 2θ values of 36.5°, 42.3°, 61.3°, and 74.2° . These peaks were assigned to the reflections from the (111), (200), (220), and (311) planes of the cubic structure of Cu_2O. The peak intensities increased with the disappearance of the peaks of the Cu phase, indicating that a single phase of Cu_2O was obtained under the deposition conditions.

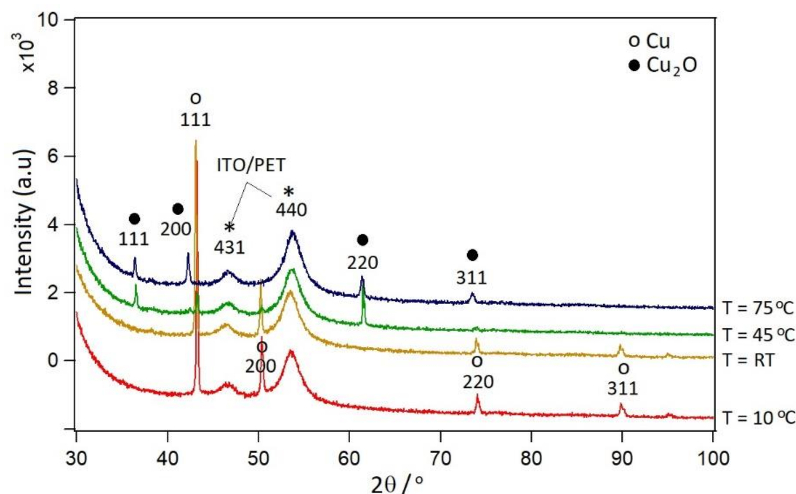

Figure 2. XRD patterns of films deposited at different temperatures.

The diffraction patterns were further analyzed by Rietveld refinement using the crystallography data analysis software GSAS. The Rietveld method involves using the least squares method to fit the measured line profile with a theoretical line profile. This method is considered the best technique for analyzing XRD patterns, especially overlapping diffraction patterns. The Rietveld method involves comparing the measured and calculated patterns, and the difference is used to improve all the structural parameters and produce a new structural model from the measured data. The diffracted intensity can be calculated based on Equation 1 [27]:

$$y_i(c) = \sum_k^i s\,|F(hkl)|^2 M_k P_k L(\theta_k) G(2\theta_i) B + y_{ib}(c) \qquad (1)$$

where s is the scale factor, $F_{(hkl)}$ is the structure factor, M_k is the multiplicity, PO_k is the preferred orientation (March-Dollase model), $L(\theta_k)$ is the Lorentz-polarization factor, $G(2\theta_i)$ is the profile geometry factor (pseudo-Voigt model), B is an isotropic temperature factor, and y_{ib} is a background factor (linear interpolation model). This analysis was used to obtain crystallographic data, including the atomic coordinates x_j, y_j, and z_j; atomic displacement parameters; unit cell dimensions; unit cell dimensions; and instrumental models, such as the angular dependence of profile parameters, FWHM and form factor, position 2θ-nol, and preferred orientation, to describe the microscopic and atomic characteristics of the thin-film crystal sample.

The crystallographic data showed that Cu has a cubic structure, an Fm-3m space group, and the lattice parameters a = b = c = 3.6150 Å. Cu has a unit cell volume of 47.2416 $Å^3$ and an atomic density of 8.9350 g/cm³. The Cu atoms at site 4a have atomic coordinates (0.0, 0.0, 0.0) and m-3m point symmetry. This structure is stable below 863 °C [1, 21]. By contrast, the cubic Cu_2O structure has a Pn-3 m space group, the lattice parameters a = b = c = 4.1685 Å, and a unit cell volume of 72.4335 $Å^3$ with an atomic density of 6.1100 g/cm³. The Cu atoms at site 4b have the atomic coordinates (1/4, 1/4, 1/4) and -3m point symmetry, whereas the O atoms at site 2a have atomic coordinates (0, 0, 0) and -43m point symmetry [28]. The residual weighted profile (Rwp) and goodness of fit (see Equation 2) were calculated by the GSAS program as suitability parameters of the match between the experimental (observed) and calculated Bragg diffraction patterns.

$$R_{wp} = \sum_i^n \left(\frac{w_i(y_i^{obs} - y_i^{calc})^2}{\sum_i^n w_i(y_i^{obs})^2} \right)^{\frac{1}{2}} \text{ and } \quad \chi^2 = \sum_i^n \frac{(y_i^{obs} - y_i^{calc})^2}{n-p} \quad (2)$$

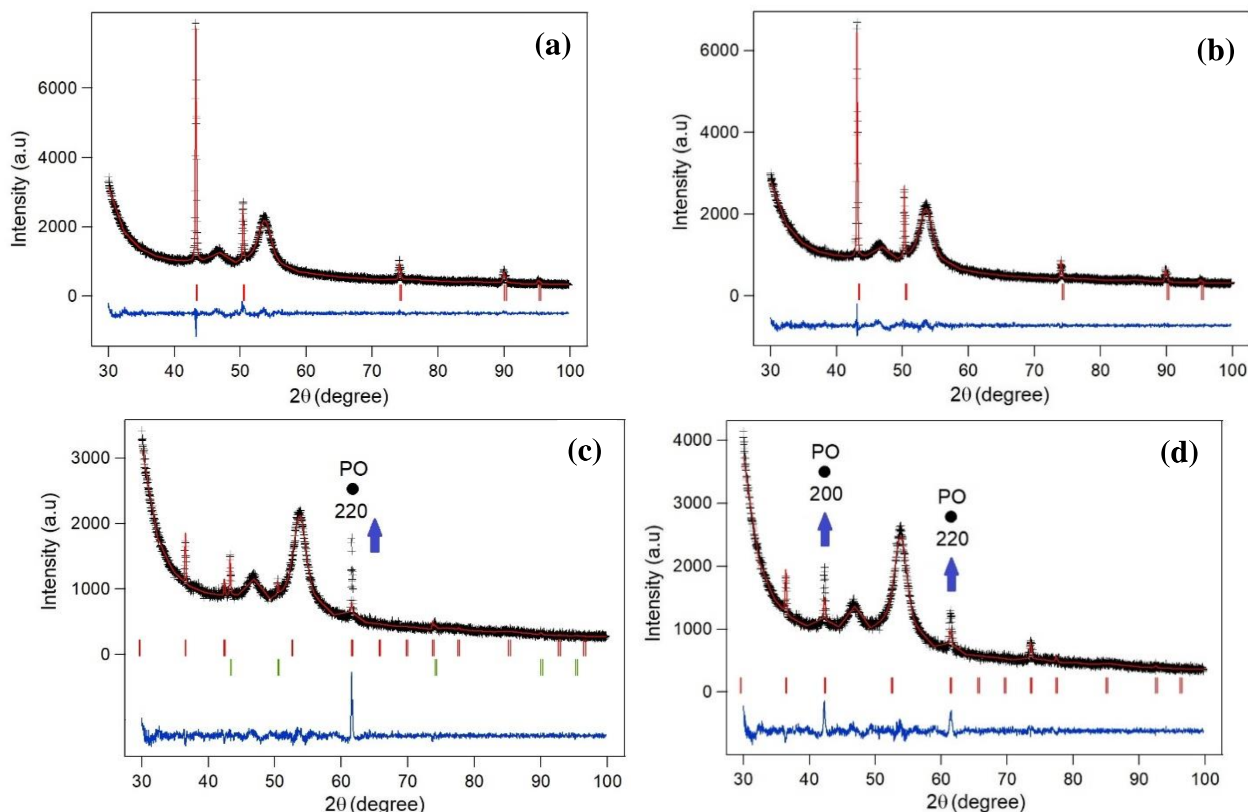

Figure 3. GSAS software results of Rietveld refinement of the XRD patterns obtained at deposition temperatures of 10°C (a), RT (b), 45°C (c), and 75°C (d).

Figure 3 shows the refinement results for the XRD patterns of the films that met the criteria for the suitability parameters Rwp and χ^2. Figures 3a-b show the refinement results for the films electrodeposited at 10°C and RT, respectively, for which the Bragg diffraction peaks corresponded to a single-phase Cu structure. Figure 3c shows the refinement results of the XRD pattern for the thin film electrodeposited at 45°C for which the Bragg diffraction peaks corresponded to two phases of Cu and Cu_2O structures. Figure 3d shows the refinement results of the XRD pattern for the thin film electrodeposited at 75°C, for which the Bragg diffraction peak corresponded to a single-phase Cu_2O structure. The quality of the fit for the XRD pattern is shown by the χ^2 curve (an ideal fit corresponds to a straight line approaching a gradient of 1): the nonlinearities for the results of the two alloys indicate preferential orientation along the [200] and [220] planes. This preferential orientation was attributed to the formation of an oriented microstructure in both XRD test samples, which was based on observations of sample microstructure observations and required confirmation. Thus, further refinement was performed using an correction factor for the preferential orientation of the diffraction intensity in the [200] and [220] directions. The powder samples did not exhibit a preferential orientation, but the presence of polycrystallinity resulted in a larger volume fraction for certain plane orientations (commonly known as texture) depending on the process used. The correction factor used in the Rietveld

refinement for this preferential orientation was based on the March-Dollase model and is shown in Equation 3 [29]:

$$P_k(\alpha) = (r^2 cos^2\alpha + \frac{1}{r} sin^2\alpha)^{\frac{3}{2}} \quad (3)$$

where α is the angle between the preferential orientation and the return-grid vector for the corrected Bragg vertex. The March r parameter was the preferential orientation index. The range of the March r parameter is $0 < r \leq 1$; thus, a decrease in r to near zero indicates an increase in the degree of preferential orientation along a particular crystallographic field direction. The relationship between the degree of preferential orientation η and the March r parameter is given in Equation 4 [29].

$$\eta = 100\% \left[\frac{(1-r)^3}{1-r^3}\right]^{\frac{1}{2}} \quad (4)$$

The XRD refinement results showed preferential orientation of the thin film samples prepared at an electrodeposition temperature of 45°C, for which r for the [220] plane was 0.33. The thin-film samples prepared at an electrodeposition temperature of 75°C preferentially oriented along the [200] and [220] planes, with r values of 0.79 and 0.21, respectively. The degree of preferential orientation, η, was 55.85% along the (220) reflection plane direction for the films electrodeposited at 45°C and 13.52% and 70.54% along the (200) and (220) reflection planes, respectively, for the films electrodeposited at 75°C. Considering the preferential orientation in the [200] crystallographic field direction improved the refinement results of the XRD pattern of the films (Fig. 4). Thus, the quality of the fit improved for patterns of films prepared at the electrodeposition temperatures of 45°C (χ^2 decreased from 2.653 to 1.383) and 75°C (χ^2 decreased from 2.280 to 1.473). The R_{wp} and goodness of fit (χ^2) for the refinement results showed an excellent fit quality for the XRD pattern. In this study, R_{wp} was defined in terms of a weighted difference between the observed and calculated XRD patterns (the ideal value of R_{wp} was less than 10%). χ^2 (chi-squared) was defined in terms of the difference between the observed and calculated XRD patterns, which was proportional to the expectation value (the ideal value of χ^2 was less than 1.3).

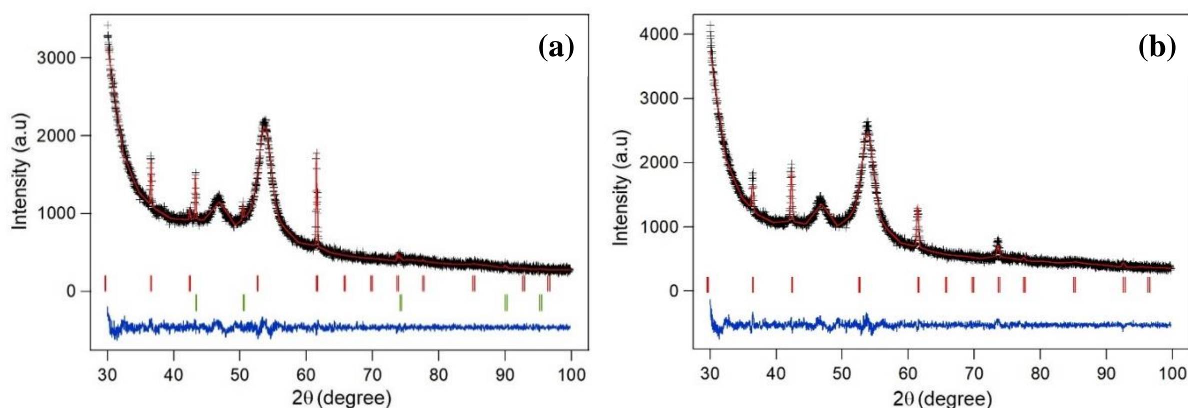

Figure 4. Results of refinement considering the preferential orientation of the XRD patterns for Cu_2O samples prepared at temperatures of 45°C (a) and 75°C (b).

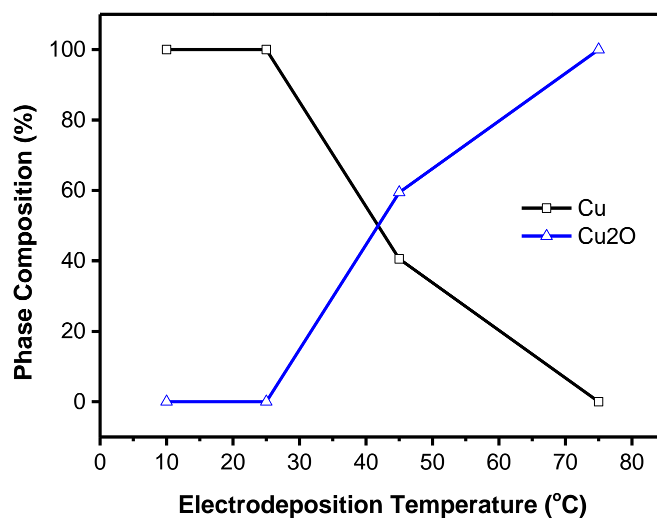

Figure 5. Phase composition of samples electrodeposited at different temperatures.

Table 1. Structural properties of Cu_2O and Cu electrodeposited at various temperatures

T(°C)	Phase	Crystal structure	Space group	Lattice parameter (Å) a	b	c	Volume (Å^3)	Density (g/cm^3)
10	Cu_2O	-	-	-	-	-		-
	Cu	Cubic	Fm-3 m	3.6113(2)	3.6113(2)	3.6113(2)	47.099(9)	8.968
RT	Cu_2O	Cubic	Pn-3 m	-	-	-		
	Cu	Cubic	Fm-3 m	3.6110(1)	3.6110(1)	3.6110(1)	47.088(8)	8.964
45	Cu_2O	Cubic	Pn-3 m	4.2594(4)	4.2594(4)	4.2594(4)	77.28(2)	6.149
	Cu	Cubic	Fm-3 m	3.613(1)	3.613(1)	3.613(1)	47.16(5)	8.949
75	Cu_2O	Cubic	Pn-3 m	4.2632(6)	4.2632(6)	4.2632(6)	77.48(3)	6.154
	Cu	-	-	-				-

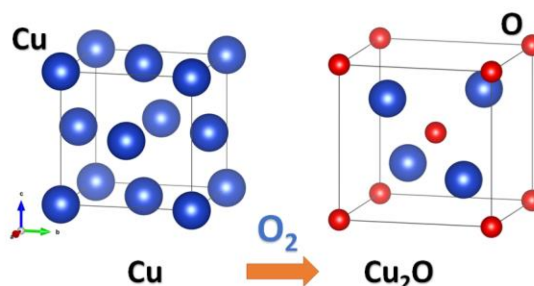

Figure 6. Crystal structure models of Cu and Cu_2O

Figure 5 shows the phase composition of samples electrodeposited at different temperatures, where a pure Cu_2O phase was obtained at a deposition temperature of 75°C. The refinement results were used to construct a crystal structure model for the thin films using VESTA software with input data from the refinement GSAS for the two alloys. The transition in the crystal structure models for the thin-film

sample between the Cu and Cu_2O phases are shown in Figure 6. All the structural parameters are summarized in Table 1.

The crystallite size and lattice strain of the films were determined by constructing a Williamson-Hall plot from the XRD peaks using Equation 5 [30]:

$$\beta \cos\theta = \frac{k\lambda}{D} + 4\varepsilon \sin\theta \qquad (5)$$

where k is the Scherrer constant (0.9), λ is the X-ray wavelength, θ is the Bragg diffraction angle, D is the crystallite size, β is the FWHM (β-instrument = 0.061°), and ε is the lattice strain. The data were fitted to a linear function y = mx + c. The lattice strain was calculated from the gradient of the straight-line (m), and the crystallite size was obtained from the linear intercept at x = 0. The measured results (Fig. 7) showed that the crystallite sizes of the thin-film samples deposited at 10 °C, RT, 45 °C, and 75 °C were 64, 52, 38, and 34 nm, respectively. The lattice strains in the thin-film samples deposited at 10 °C, RT, 45 °C, and 75 °C were 0.000015, 0.00023, 0.00047, and 0.00024 nm, respectively. Increasing the electrodeposition temperature for the thin-film samples reduced the crystallite size, and the lattice strain increased when the sample underwent an oxidation transition from the Cu to Cu_2O phase. Thus, oxygen binding restrained the rate of grain growth in the thin-film samples, and the preferential orientation in the [200] and [220] crystallographic plane directions induced a stress in the crystal, which caused the lattice strain to increase when the sample underwent the oxidation transition.

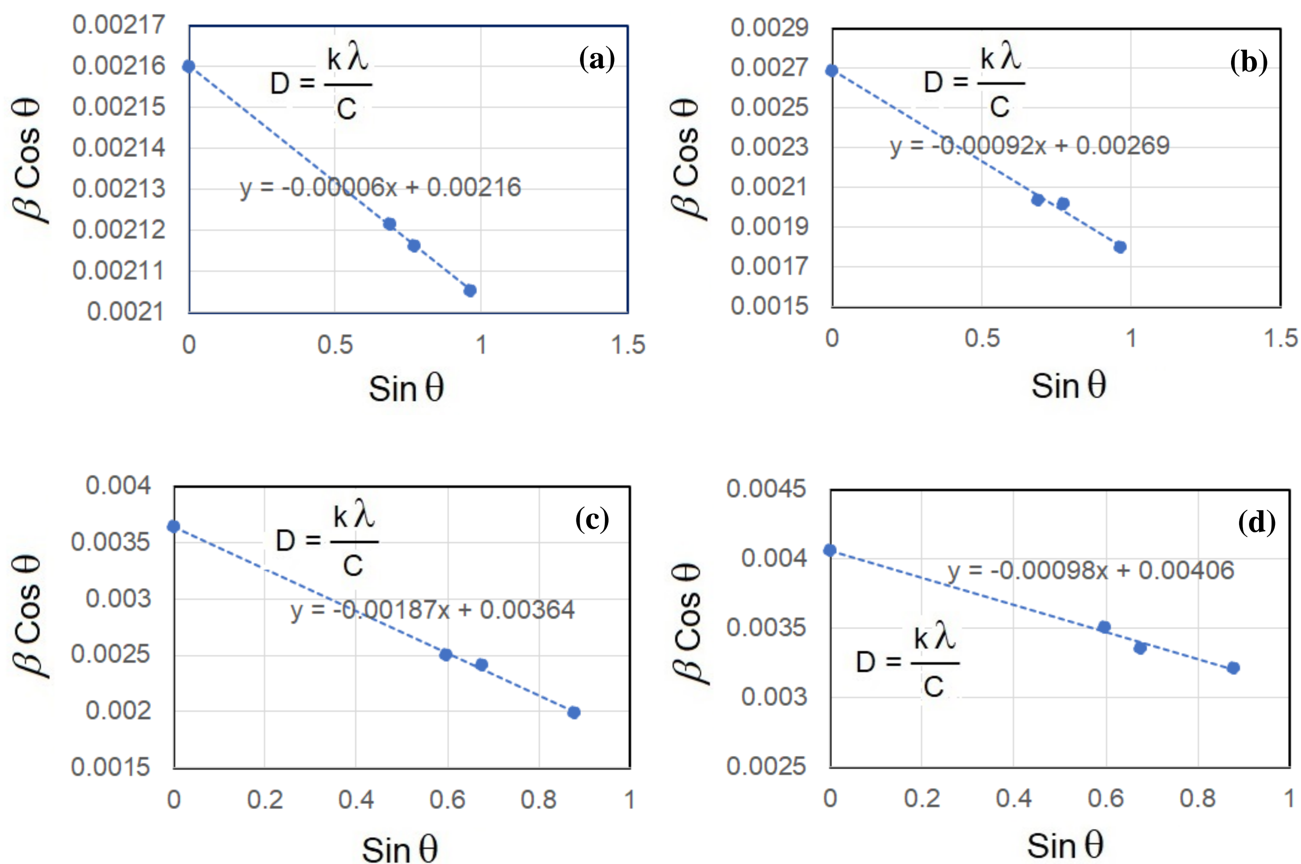

Figure 7. Williamson-Hall plots used to determine the crystallite size and lattice strain of samples electrodeposited at temperatures of 10°C (a), RT (b), 45°C (c), and 75°C (d).

To determine the optical properties of the electrodeposited Cu_2O, films containing the Cu_2O phase were analyzed using a UV–vis spectrophotometer equipped with a diffuse-reflectance sphere. The band gap energy was obtained from the Tauc plot shown in Figure 8. The direct band gap energy values of Cu_2O deposits prepared at 45°C and 75°C were 2.07 eV (Fig. 8a) and 2.18 eV (Fig. 8b), respectively. These values lie within the band gap energy range of a Cu_2O semiconductor (between 1.9 eV and 2.2 eV [18,31]. The difference in the measured band gap energies of the two samples was attributed to the composition of the deposit. The bandgap energy was decreased by the presence of metallic Cu, as shown by the quantitative phase analysis of the XRD pattern (Fig. 2) for the sample prepared at 45°C. The pure Cu_2O sample exhibited a high band gap energy.

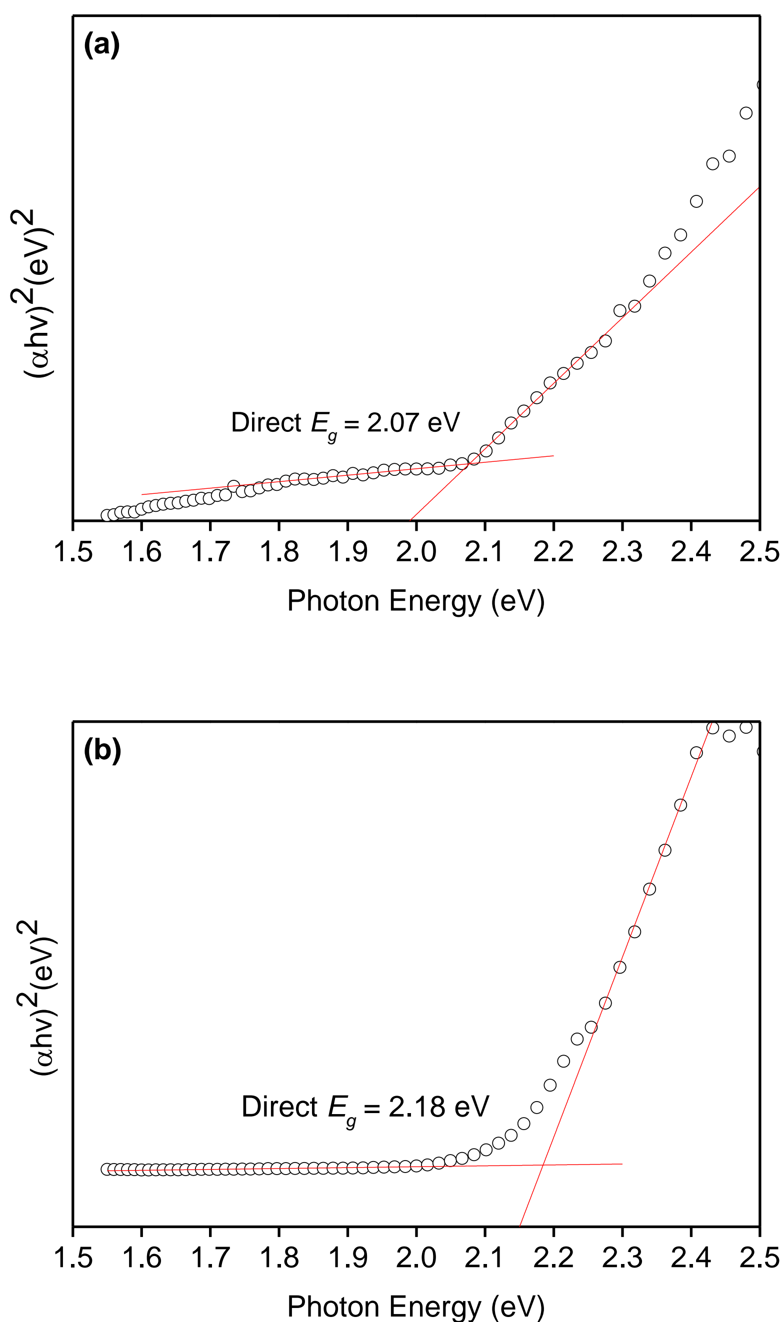

Figure 8. Tauc plots of Cu_2O samples prepared at 45°C (a) and 75°C (b).

4. CONCLUSION

In this study, Cu_2O films were synthesized by ammonium-sulfate-assisted electrodeposition at different temperatures. A Cu_2O phase formed along with metallic Cu at a deposition temperature of 45°C. A pure nanocrystalline Cu_2O film was successfully produced at 75°C. Rietveld refinement results obtained using GSAS software showed that an increase in the deposition temperature reduced the crystallite size and increased the lattice strain. Oxygen binding occurred during the formation of the oxide phase and was considered to restrain crystallite growth, producing fine Cu_2O grains. The Cu_2O structure preferentially oriented along the (200) and (220) reflection planes at high deposition temperatures due to the deposition of oriented microstructure films. This preferred orientation induced stress in the crystal that contributed to an increase in the lattice strain.

ACKNOWLEDGEMENT
Financial support for this study was provided by Universitas Negeri Jakarta and Direktorat Riset dan Pengabdian Masyarakat Kemenristek-BRIN of the Republic of Indonesia under the Research Scheme Penelitian Dasar Unggulan Perguruan Tinggi (DUPT) (31/SP2H/DRPM/LPPM/III/2020).

DATA AVAILABILITY STATEMENT
The raw data presented in this paper are being used in ongoing research and cannot be shared at this time but are available upon reasonable request.

References

1. M. Bagherzadeh, N. Mousavi, M. Amini, S. Gautam, J.P. Singh, K.H. Chae, *Chinese Chem. Lett.*, 28 (2017) 1125–1130.
2. Y. Su, A. Nathan, H. Ma, H. Wang, *RSC Adv.*, 6 (2016) 78181–78186.
3. I. Akhirudin, S. Budi, Yusmaniar, *J. Phys. Conf. Ser.*, 1428 (2020).
4. B. Rajesh Kumar, B. Hymavathi, T. Subba Rao, *Mater. Today Proc.*, 4 (2017) 3903–3910.
5. S.S. Sawant, A.D. Bhagwat, C.M. Mahajan, *J. Nano- Electron. Phys.*, 8 (2016) 1–5.
6. K. Chen, S. Song, D. Xue, *CrystEngComm*, 17 (2015) 2110–2117.
7. K.I. Ozoemena, S. Momeni, *J. Am. Chem. Soc.*, 170 (2018) 10356–10357.
8. O. Messaoudi, I. Ben Assaker, M. Gannouni, A. Souissi, H. Makhlouf, A. Bardaoui, R. Chtourou, *Appl. Surf. Sci.*, 366 (2016) 383–388.
9. A.H. Alami, A. Allagui, H. Alawadhi, *Renew. Energy*, 82 (2014) 21–25.
10. G.F. Pan, S. Bin Fan, J. Liang, Y.X. Liu, Z.Y. Tian, *RSC Adv.*, 5 (2015) 42477–42481.
11. M. Abdelfatah, J. Ledig, A. El-Shaer, A. Sharafeev, P. Lemmens, M.M. Mosaad, A. Waag, A. Bakin, *ECS J. Solid State Sci. Technol.*, 5 (2016) Q183–Q187.
12. X. Jiang, Q. Lin, M. Zhang, X. Song, Z. Sun, *Optik (Stuttg).*, 126 (2015) 5544–5547.
13. S. Budi, D. Indrawati, M. Arum, *AIP Conf. Proc.*, 2342 (2021) 1–6.
14. S. Budi, B. Kurniawan, D.M. Mott, S. Maenosono, A.A. Umar, A. Manaf, *Thin Solid Films*, 642 (2017) 51–57.
15. M. Xiong, D.G. Ivey, *Electrochim. Acta*, 260 (2018) 872–881.
16. S. Rezalou, T. Öznülüer, Ü. Demir, *Appl. Surf. Sci.*, 448 (2018) 510–521.
17. S. Budi, A.R. Daud, S. Radiman, A.A. Umar, *Appl. Surf. Sci.*, 257 (2010) 1027–1033.
18. G. Wu, W. Zhai, F. Sun, W. Chen, Z. Pan, W. Li, *Mater. Res. Bull.*, 47 (2012) 4026–4030.
19. F. Ye, C. Xu, G. Liu, M. Yuan, Z. Wang, X. Du, J.K. Lee, *Energy Convers. Manag.*, 160 (2018)

85–92.
20. M. Hong, D. Jin, J. Soo, *Thin Solid Films*, 489 (2005) 122–129.
21. S.A. Razali, S.R. Majid, *Mater. Des.*, 153 (2018) 24–35.
22. Y. Lin, H. Zhang, W. Deng, D. Zhang, N. Li, Q. Wu, C. He, *J. Power Sources*, 384 (2018) 278–286.
23. M.J. Siegfried, K. Choi, *J. Am. Chem. Soc.*, 128 (2006) 10356–10357.
24. B.H. Toby, *J. Appl. Crystallogr.*, 34 (2001) 210–221.
25. M.S. Idris, R.A.M. Osman, *Adv. Mater. Res.*, 795 (2013) 479–482.
26. V.Y. Zenou, S. Bakardjieva, *Mater. Charact.*, 144 (2018) 287–296.
27. V.K. Pecharsky, P.Y. Zavalij, Fundamentals of Powder Diffraction and Structural Characterization of Materials, Springer Science+Business Media, (2005).
28. R. Wyckoff, Crystal Structures 1, Interscience Publisher, (1963) New York.
29. E. Zolotoyabko, *J. Appl. Crystallogr.*, 42 (2009) 513–518.
30. D. Nath, F. Singh, R. Das, *Mater. Chem. Phys.*, 239 (2020) 122021.
31. J. Li, N. Wu, *Catal. Sci. Technol.*, 5 (2015) 1360–1384.

© 2022 The Authors. Published by ESG (www.electrochemsci.org). This article is an open access article distributed under the terms and conditions of the Creative Commons Attribution license (http://creativecommons.org/licenses/by/4.0/).